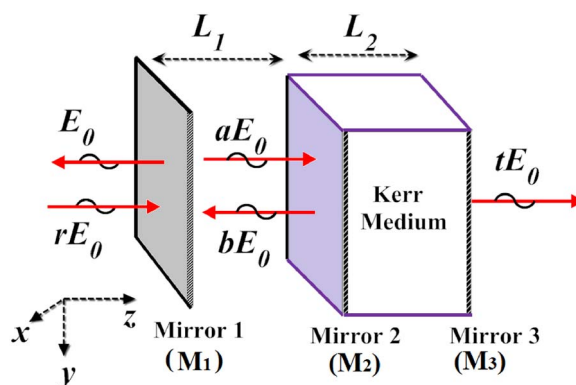# On the Maxwell-Duffing Approach to Model Photonic Deflection Sensor

Abdelbaset M. A. Ibrahim
P. K. Choudhury, Senior Member, IEEE

On the Maxwell-Duffing Approach to Model Photonic Deflection Sensor

Abdelbaset M. A. Ibrahim[1] **and P. K. Choudhury,**[2] *Senior Member, IEEE*

[1]School of Physics, Faculty of Applied Sciences, University Technology MARA,
40450 Selangor, Malaysia
[2]Institute of Microengineering and Nanoelectronics, Universiti Kebangsaan Malaysia,
43600 Selangor, Malaysia

Abstract: This paper deals with the conceptualization of Maxwell-Duffing theory to model photonic deflection sensor along with functionality, which is based on the phenomena of optical bi- and multistabilities. The sensing system is considered to be consisting of Kerr nonlinear material along with suitably positioned mirrors. The efficacy of the approach is emphasized through a series of numerical simulations, and the reliability of the system is discussed. Effects due to system memory and periodicity in the optical bistability threshold have been demonstrated. It has been found that the approach provides a powerful tool to study optical bistability in resonating structures, particularly for materials with large third-order nonlinearity and for operating frequencies near the natural resonance of the material.

Index Terms: Photonic deflection sensor, Kerr nonlinearity, optical bistability.

1. Introduction

Investigators have reported varieties of application oriented optical sensors in the literature [1]–[4]. Among those, the use of optical bi- and multistabilities in sensing has been of great interest. Pivoted to this concept, photonic deflection sensing [5]–[6] techniques implementing a nonlinear Fabry-Perot (FP) resonator filled with third-order nonlinear medium have been on research frontline. The functionality of such sensors essentially relies on the ability of mirror(s) used in the resonator system to deflect light in response to an externally applied force. The deflection (or deviation) of mirror (due to the external force) from its original position results in a *shift* of the output signal, thereby determining the sensing capability of the system.

Scientific basis of the involved nonlinear process can be modeled using theories in optics [7]–[9]. However, an alternative approach to model functionality and performance of the device can also be thought about. Within the context, the *Maxwell-Duffing* approach remains vital in modeling a special class of optical bistability, especially those of the intrinsic-type [10] and for highly nonlinear material [11]. This approach employs the Duffing anharmonic oscillator equation as a new constitutive relation instead of Taylor series expansion, as used in the *usual* approach. More explicitly, the usual approach employs the nonlinear polarization P to be expanded in terms of the electric field E using Taylor series, and the wave equation is solved for E as the dependent variable. In contrast, the *Maxwell-Duffing* approach implements the electric field of the wave equation to be expressed as a nonlinear function of the polarization P using the Duffing anharmonic equation, and the resulting nonlinear polarization equation is solved for P rather than E. The latter approach provides a powerful tool to study optical bistability in previously mentioned resonating structures for three

reasons: i) It accounts for both the extrinsic and the intrinsic types of bistability while the usual approach accounts for the extrinsic type only. (The driving field in Maxwell-Duffing approach is treated as dependent on the material response, i.e., $E = E(P)$, as was first realized by Duffing in his work on the classical anharmonic oscillator [12].) It must be noted that the extrinsic type of bistability results from the extrinsic feedback mechanism provided by the partially reflecting resonator mirror [13]–[16], while the intrinsic type results from the non-unique feedback mechanism of molecules to the driving field in microscopic domain [17], [18]. ii) For materials with large nonlinearity, or if the operating wavelength lies in the neighborhood of material resonance where the nonlinear material usually exhibits huge third order nonlinearity [19], the usual constitutive relation becomes questionable since the *undepleted wave approximation* is clearly violated. iii) The approach does not require the exact nature of nonlinear susceptibility $\chi^{(3)}$ of material because nonlinearity of system is automatically contained in the induced polarization [20]–[21].

In our proposed configuration, the Fabry-Perot resonator is filled with an insulating solid nonlinear crystal driven by an infrared laser source. However, the use of solid, instead of liquid, in a Fabry-Perot system provides higher durability and better stability. Furthermore, the use of infrared (IR) laser source together with an infrared active nonlinear crystal provides additional advantages such as, fast measurement as it propagates with the speed of light, and very small characteristic time constants of the measurement process. This infrared photonic sensor is strongly wavelength-dependent, and the highest detectivity is obtained when the operating frequency ω of the driving laser source lies within the natural resonance frequency ω_0 of the nonlinear medium. This is because the nonlinear response of material in this region becomes very large and resonant. Hence, such a proposed device becomes highly sensitive to changes in optical path length produced by the movable mirror, as well as to effective index variations of the resonator. In the present communication, we make an attempt to utilize the Maxwell-Duffing approach to investigate the functionality and reliability of photonic deflection sensor based on the phenomenon of optical bi- and multistabilities. A mathematical formulation is made of the resonating system followed by numerical simulations. Investigations in respect of performance and sensing capability of the device under consideration reveal that the system possesses memory effects through remembering previous deflections. In addition, the threshold value of optical bistability depicts a periodic pattern as a function of the applied deflection. The sensitivity of the device in response to the applied deflection is mainly discussed in this paper.

2. Mathematical Formulation

2.1. Field Inside the Nonlinear Medium

We consider a nonlinear dielectric material modeled as a system consisting of classical anharmonic oscillators, where each oscillator has mass m undergoing a damped motion when acted upon by a nonlinear restoring force and a periodic external force. The response of Kerr nonlinear medium to the EM waves may be described by the time t-dependent nonlinear Duffing equation of motion

$$\frac{\partial^2 P}{\partial t^2} + \Gamma \frac{\partial P}{\partial t} + \omega_0^2 P + \beta P^3 = \gamma E. \tag{1}$$

In (1), $P(z, t)$, and $E(z, t)$ are, respectively, the induced macroscopic polarization and the driving electric field. Also, Γ, β and γ are damping, nonlinear and coupling constants, respectively. Furthermore, the term $\Gamma(\partial P/\partial t)$ represents the linear loss and ω_0 is the resonance frequency. Assuming both the driving field and the induced polarization are time-harmonic plane waves propagating along the z-direction, we can have

$$E(z, t) = \frac{1}{2}[E(z)\exp(-i\omega t) + E^*(z)\exp(+i\omega t)] \tag{2}$$

$$P(z, t) = \frac{1}{2}[P(z)\exp(-i\omega t) + P^*(z)\exp(+i\omega t)]. \tag{3}$$

In (2) and (3), ω is the angular frequency of wave in the unbounded medium. Now, the substitution of (2) and (3) into (1) yields the time-independent Duffing nonlinear equation as

$$E = \frac{1}{\gamma}\left[\left(\omega_0^2 - \omega^2 - i\omega\Gamma\right) + 3\beta|P|^2\right]P. \tag{4}$$

It is to be noted that (4) is derived under the single-frequency approximation where the third-harmonic term is ignored. If the electric field is y-polarized, the magnetic field inside Kerr medium may then be written as

$$H_x(z) = \frac{i}{\gamma\omega\mu_0}\left[\left(\omega_0^2 - \omega^2 - i\Gamma\omega\right)\frac{dP}{dz} + 3\beta\left(P^2\frac{dP^*}{dz} + 2|P|^2\frac{dP}{dz}\right)\right]. \tag{5}$$

At the high frequency limit, the wave equation for a plane polarized monochromatic field propagating along the z-direction is

$$\frac{d^2E_x}{dz^2} = -\frac{\omega^2}{c^2}\varepsilon_\infty E_x + \mu_0\omega^2 P \tag{6}$$

where c and μ_0 are, respectively, the speed of light and the free-space magnetic permeability. Here, ε_∞ is the high-frequency limit of complex dielectric function $\varepsilon(\omega)$. Substituting (2) in (6), after some mathematical steps, we get the following nonlinear differential equation in terms of polarization:

$$\left[|\rho|^2 + 2\beta(\rho + \rho^*)|P|^2 + 3\beta^2|P|^4\right]\frac{d^2P}{dz^2} = -2\beta\left[\rho^* + 2\beta|P|^2\right]P^*\left(\frac{dP}{dz}\right)^2 + 2\beta^2 P^3\left(\frac{dP^*}{dz}\right)^2$$

$$- 4\beta\left[\rho^* + \beta|P|^2\right]P\frac{dP}{dz}\frac{dP^*}{dz} - \varepsilon_\infty\omega^2\left[\rho^*(\rho + \Omega^2) + \beta(2\rho + \Omega^2)|P|^2 + \beta^2|P|^4\right]P \tag{7}$$

where $\rho = \Delta - i\omega\Gamma = \omega_0^2 - \omega^2 - i\omega\Gamma$, ρ^* is the complex conjugate of ρ, and $\Omega^2 = \omega_L^2 - \omega_0^2$ is a measure of reststrahlen width between longitudinal optical (LO) and transverse optical (TO) frequencies ω_L and ω_0. Equation (7) is an ordinary differential equation, which may be integrated numerically as an initial value problem, in order to evaluate the desired polarization.

2.2. Sensor Analysis

Fig. 1 illustrates the schematic diagram of sensor system consisting of four mediums 1, 2, 3, and 4 with their respective refractive index (RI) values as n_1, n_2, n_3, and n_4. In this figure, M_1, M_2 and M_3 are the three mirrors, and L_1 and L_2 are the separations, as shown. Considering the propagation of EM waves along the $+z$-direction, fields in Kerr nonlinear medium 3 assume the forms as described by (4) and (5). We consider EM fields in the mediums 1, 2, and 4 to be as

$$E_1 = E_x^i(z,t) + E_x^r(z,t) = E_0\exp(ik_1z) + rE_0\exp(-ik_1z) \tag{8}$$

$$E_2 = E_x^a(z,t) + E_x^b(z,t) = aE_0\exp(ik_2z) + bE_0\exp(-ik_2z) \tag{9}$$

$$E_4 = E_x^t(z,t) = tE_0\exp(ik_4z) \tag{10}$$

$$H_1 = H_y^i + H_y^r = (k_1/\omega\mu_0)E_0\exp(ik_1z) - (k_1/\omega\mu_0)rE_0\exp(-ik_1z) \tag{11}$$

$$H_2 = H_y^a + H_y^b = (k_2^z/\omega\mu_0)aE_0\exp(ik_2^zz) - (k_2^z/\omega\mu_0)bE_0\exp(-ik_2^zz) \tag{12}$$

$$H_4 = H_y^t(z,t) = (k_4/\omega\mu_0)tE_0\exp(ik_4z) \tag{13}$$

where the suffixes indicate the situations in the respective mediums: In these equations, E_0 is electric field amplitude, and r and t are complex reflection and transmission coefficients, respectively. Also, a and b are, respectively, forward and backward coefficients in the medium 2. Moreover, the coefficients k_1, k_2, and k_4 are, respectively, the wavenumbers in mediums 1, 2, and 4.

Now, the coefficients r and t can be evaluated by applying suitable boundary conditions for both electric and magnetic fields at each interface following the standard analysis in linear optics [22].
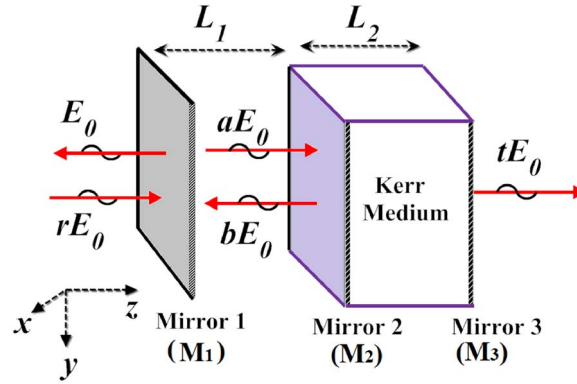
Fig. 1. Schematic diagram of photonic deflection sensor.

However, the existence of mirrors at these boundaries modifies the continuity conditions to the following forms [11], [20], [23] as

$$E_1(z = -L_1) = E_2(z = -L_1) \tag{14}$$

$$H_1(z = -L_1) = H_2(z = -L_1) + \eta_1 E_2(z = -L_1) \tag{15}$$

$$E_2(z = 0) = E_3(z = 0) \tag{16}$$

$$H_2(z = 0) = H_3(z = 0) + \eta_2 E_3(z = 0) \tag{17}$$

$$E_3(z = L_2) = E_4(z = L_2) \tag{18}$$

$$H_3(z = L_2) - H_4(z = L_2) = \eta_3 E_4(z = L_2). \tag{19}$$

In (15), (17), and (19), the parameter $\eta_i = \delta_{Mi}(\sigma_{Mi} - i\omega\varepsilon_0\varepsilon_{Mi})$ represents mirror coefficient with the subscript i as the mirror number (e.g., M_1, M_2, and M_3). The coefficients σ_M, δ_M and ε_M are, respectively, conductivity, thickness, and dielectric permittivity of mirror materials.

In this paper, we may assume the second and the third resonator mirrors to be identical (i.e., $\eta_2 = \eta_3$) while the movable mirror with coefficient η_1 assumes different values. If we assume that the mirrors are made of perfect dielectric material with $\sigma_M = 0$, η_i reduces to the form $\eta_i = -i\omega\varepsilon_0\delta_{Mi}\varepsilon_{Mi}$. In such a case, wave propagates into the mirror material without attenuation, and the electric/ magnetic fields are in phase (as in free-space) but with ε_0 replaced with $\varepsilon_M = \varepsilon_0\varepsilon_M$. Such a coated mirror can be designed to meet the required reflectance at the optimized wavelength using various metallic or dielectric materials. Since η_i has no direct physical significance, the illustrative plots in this work are labeled with the parameter η_i and its equivalent power reflectivity R_M, i.e., the reflectivity of a mirror placed at the boundary between two mediums under linear approximation (as will be explained in the following section). The substitution of (4), (5), and (8)–(13) into (14)–(19) yields the following algebraic equations:

$$r\delta_1^+ = a\delta_2^- + b\delta_2^+ - \delta_1^- \tag{20}$$

$$k_1\delta_1^- - k_1 r\delta_1^+ = k_2 a\delta_2^- - k_2 b\delta_2^+ + \omega\mu_0\eta_1\left[a\delta_2^- + b\delta_2^+\right] \tag{21}$$

$$aE_0 + bE_0 = (1/\gamma)\left[(\Delta - i\omega\Gamma)P_1 + (3/4)\beta|P_1|^2 P_1\right] \tag{22}$$

$$\gamma k_2[a-b]E_0 = i\left[(\Delta - i\omega\Gamma) + \frac{3}{2}\beta|P_1|^2\right]\frac{dP_1}{dz} + i\frac{3}{4}\beta P_1^2\frac{dP_1^*}{dz} + \omega\mu_0\eta_2\left[(\Delta - i\omega\Gamma) + \frac{3}{4}\beta|P_1|^2\right]P_1 \tag{23}$$

$$\gamma t E_0\delta_4^+ = (\Delta - i\omega\Gamma)P_2 + \frac{3}{4}\beta|P_2|^2 P_2 \tag{24}$$

$$\gamma[k_4 + \omega\mu_0\eta_3]t E_0\delta_4^+ = i(\Delta - i\omega\Gamma)\frac{dP_2}{dz} + i\frac{3}{4}\beta\left[P_2^2\frac{dP_2^*}{dz} + 2|P_2|^2\frac{dP_2}{dz}\right]. \tag{25}$$

In (20)–(25), the quantities P_1 and P_2 and their derivatives are the polarization values at the boundaries $z = 0$ and $z = L_2$, respectively; they are related through numerical integration, as will be explained in the Appendix. The different symbols have meanings as

$$\delta_1^+ = \exp(ik_1 L_1), \ \delta_1^- = \exp(-ik_1 L_1), \ \delta_2^- = \exp(-ik_2 L_1), \ \delta_2^+ = \exp(ik_2 L_1), \ \text{and} \ \delta_4^+ = \exp[ik_4 L_2].$$

Upon solving (20)–(23), we get expressions corresponding to the complex reflection coefficient r and the incident electric field intensity E_0. Now, either (24) or (25) may be used to evaluate the complex transmission coefficient t. Furthermore, (24) and (25) may be solved to obtain the expression for polarization derivative dP_2/dz at the last boundary ($z = L_2$). It can be shown that the expressions for r, E_0, t and dP_2/dz will ultimately have their forms as follows:

$$r = \left[\frac{2k_1 - \hbar_1^-}{\hbar_1^-}\right]\frac{\delta_1^-}{\delta_1^+} - \frac{1}{\delta_1^+}\left[\frac{2k_2}{\hbar_1^- \delta_2^+ - \hbar_1^+ \delta_2^-}\right]\left[\frac{1}{\gamma E_0}\left(\rho P_1 + \frac{3}{4}\beta|P_1|^2 P_1\right) - 2\frac{k_1}{\hbar_1^-}\frac{\delta_1^-}{\delta_2^+}\right] \tag{26}$$

$$E_0 = \frac{-1}{4\gamma k_1 k_2 \delta_1^-}\left\{ i(\hbar_1^- \delta_2^+ - \hbar_1^+ \delta_2^-)\left[\frac{3}{4}\beta P^2 \frac{dP_1^*}{dz} + \rho \frac{dP_1}{dz} + \frac{3}{2}\beta|P_1|^2 \frac{dP_1}{dz}\right]\right.$$
$$\left. + \left[\omega\mu_0\eta_2(\hbar_1^- \delta_2^+ - \hbar_1^+ \delta_2^-) - k_2(\hbar_1^- \delta_2^+ + \hbar_1^+ \delta_2^-)\right]\left[\rho P_1 + \frac{3}{4}\beta|P_1|^2 P_1\right]\right\} \tag{27}$$

$$t = \frac{1}{\gamma E_0 \delta_4^+}\left[\rho P_2 + (3/4)\beta|P_2|^2 P_2\right] \tag{28}$$

$$\frac{dP_2}{dz} = -iP_2\left\{\frac{3}{4}\beta(k_4 + \omega\mu_0\eta_3^*)\left[\rho^* + \frac{3}{4}\beta|P_2|^2\right]|P_2|^2 + (k_4 + \omega\mu_0\eta_3)\left[\rho^* + \frac{3}{2}\beta|P_2|^2\right]\left[\rho + \frac{3}{4}\beta|P_2|^2\right]\right\}$$
$$\bigg/ \left\{\left[\rho + \frac{3}{2}\beta|P_2|^2\right]\left[\rho^* + \frac{3}{2}\beta|P_2|^2\right] - \frac{9}{16}\beta^2|p_2|^4\right\} \tag{29}$$

where $\hbar_1^- = (k_1 - k_2 + \omega\mu_0\eta_1)$ and $\hbar_1^+ = (k_1 + k_2 + \omega\mu_0\eta_1)$.

For convenience in numerical simulation, (7) and (26)–(29) may be cast into a dimensionless form. For this reason, we introduce new scaled variables as follows:

$$f = \omega/\omega_0, \ u = z\omega_0/c, \ g = \Gamma/\omega_0, \ E_s = E_0/E_0, \ p = P/P_0, \ \beta_s = \beta P_0^2/\omega_0^2, \ \gamma_s = \gamma E_0/\omega_0^2 P_0$$
$$= \omega_p^2/\omega_0^2 \tag{30}$$

where the resonance frequency ω_0 of material gives a natural scaling for thickness or deflection, damping parameter and frequency. In a similar fashion, both the electric field incident amplitude E_0 and the polarization P are scaled using *typical* values E_0 and P_0, respectively. The scaling values P_0 and E_0 are conveniently chosen for polarization and electric field based on the linear relationship $P_0 = \varepsilon_0 E_0$ in free-space. The scaling procedure and the implemented numerical strategy are summarized in the Appendix.

3. Results and Discussion

3.1. Dielectric Mirrors

We now make an attempt to draw a connection between the mirror coefficient η and the equivalent value of the mirror reflectivity R_M. In our system, it can be shown that for a mirror M placed at the boundary between the mediums i and j has reflectivity given as [24]

$$R_M = \rho_{ji}\rho_{ji}^* = \frac{(n_j - n_i)^2 - \eta_s^*(n_j - n_i) - \eta_s(n_j - n_i) + |\eta_s|^2}{(n_j + n_i)^2 + \eta_s^*(n_j + n_i) + \eta_s(n_j + n_i) + |\eta_s|^2} \tag{31}$$

where η_s is mirror parameter and ρ_{ji} is elementary linear coefficient between the mediums i and j. Due to the existence of mirror at the boundary [23], ρ_{ji} and its complex conjugate ρ_{ji}^*

are modified to the form

$$\rho_{ji} = \frac{[n_i - n_j - \eta_s]}{[n_i + n_j + \eta_s]}, \quad \rho_{ji}^* = \frac{[n_i - n_j - \eta_s^*]}{[n_i + n_j + \eta_s^*]}. \tag{32}$$

In our system, $n_1 = n_2 = n_4 = 1$ (i.e., free-space). Further, the linear RI n_3 of nonlinear medium may be evaluated from the following formula corresponding to the multiple oscillator model for linear dielectric susceptibility [25]

$$\varepsilon(\omega) = \varepsilon'(\omega) + i\varepsilon''(\omega) = \left[\varepsilon_\infty + \frac{\varepsilon_{stj}\omega_{0j}^2}{\omega_{0j}^2 - \omega^2 - i\omega\Gamma_j} \right] \tag{33}$$

where $\varepsilon'(\omega)$ and $\varepsilon_r''(\omega)$ are real and imaginary parts of linear dielectric function, respectively. The coefficient ε_{stj} is oscillator strength of the j resonance and the refractive index is given by $n_3 = \sqrt{\varepsilon'(\omega)}$. The Duffing anharmonic oscillator model represented by (1) is typically suitable for an insulating ionic crystal with Kerr nonlinear response in the infrared (IR) spectrum. Therefore, the input parameters consistent with IR spectrum have to be employed in numerical analysis. Taking MgO as an example, it has three prominent resonances within the range 2–150 THz. They occur at 4.26×10^{12} Hz (142 cm^{-1}), 7.68×10^{12} Hz (256 cm^{-1}) and 12.18×10^{12} Hz (406 cm^{-1}) with the strongest resonance occurring at 12.18×10^{12} Hz. We follow the SI units and adopt the fitting parameters associated with these resonances for bulk MgO crystal, as in [26]. These parameters are $\varepsilon_\infty = 3.01$, $\varepsilon_{st1} = 0.055$, $\varepsilon_{st2} = 0.11$, $\varepsilon_{st3} = 3.2$, $\Gamma_1/\omega_0 = 0.7$, $\Gamma_2/\omega_0 = 0.2$ and $\Gamma_3/\omega_0 = 0.02$. Hence, (33) yields an average value of RI $n_3 = 11.05$ at the frequency $\omega = 11.836 \times 10^{12}$ Hz or at $\omega = 0.98\omega_0$ where $\omega_0 = 12.18 \times 10^{12}$ Hz. This high value of linear RI is expected as the real part of linear dielectric function is high and positive in the region just below the resonance frequency.

Fig. 2 illustrates the relationship between η_s and R_M, as derived by using (31). For the first mirror M$_1$, real and imaginary parts (η_{s1a}, η_{s1b}) are represented by red and black lines, respectively, while for M$_2$ = M$_3$ mirrors, real and imaginary parts (η_{s2a}, η_{s2b}) are represented by blue and magenta lines, respectively. For the first mirror M$_1$, we may choose a pure thin metallic sheet, which means that the desired reflectivity R_{M1} of the mirror is mapped with the values of η_{s1a} on the red curve. In this paper, we have chosen $\eta_{s1a} = 12$, which corresponds to a reflectivity of $R_{M1} = 0.75$. For Fabry-Perot mirrors (M$_2$ = M$_3$), we may consider a pure dielectric coating which means that the desired reflectivity of these mirrors $R_{M2} = R_{M3}$ is mapped with η_{s2b} values on the magenta curve. For these mirrors we have chosen $\eta_{s2b} = 25$, which corresponds to the reflectivity value $R_{M2} = R_{M3} = 0.94$.

3.2. Material Aspects

Even though the current Maxwell-Duffing approach is valid for any ionic crystal in the far-infrared region, it is rather appropriate to use input parameters for specific material. The scaling value for electric field is conveniently chosen to be $E_0 = 10^7$ V/m—the minimum value required to invoke the nonlinear response in these materials [8]. To determine the value of scaling polarization P_0, we use the relationship $P_0 = \varepsilon_0 E_0$ in free space, i.e., $P_0 = 10^7 \varepsilon_0 = 8.854 \times 10^{-5}$ C/m^2. To calculate the parameter $w^2 = \omega_p^2/\varepsilon_\infty\omega_0^2$, we first evaluate plasma frequency from the formula $\omega_p^2 = \varepsilon_\infty(\omega^2 - \omega_0^2)$ [25]. This gives $\omega_p = 4.2 \times 10^{12}$ Hz, and eventually we obtain $w^2 = 0.0396$ for bulk MgO crystal. In this case, the scaled coupling parameter $\gamma_s = \gamma E_0/\omega_0^2 P_0 = \omega_p^2/\omega_0^2 = 0.1192$. The damping parameter Γ may be evaluated from the full-width at half maximum (FWHM) of the imaginary part of linear dielectric function $\varepsilon_r''(\omega)$ for bulk MgO crystal. By plotting (33), we have found $2\Gamma = 0.06 \times 10^{12}$ Hz, which yields a scaled damping value $g = \Gamma/\omega_0 = 0004926$. Finally, the nonlinear coefficient β is estimated from the following equation for Kerr nonlinearity [27]:

$$\beta = \frac{4}{9\gamma^3}\varepsilon_0\chi^{(3)}\left(\omega_0^2 - \omega^2 + i\omega\Gamma\right)\left(\omega_0^2 - \omega^2 - i\omega\Gamma\right)^3 \tag{34}$$
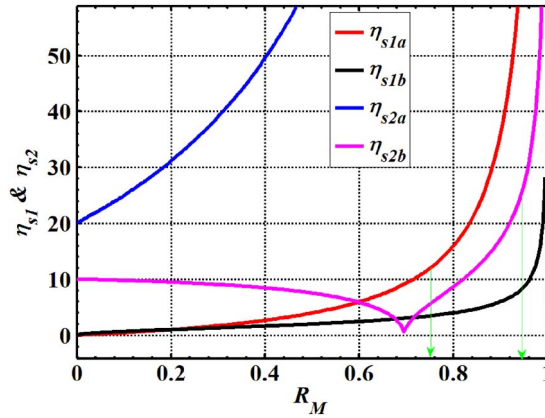
Fig. 2. Plot of complex mirror coefficients η against the equivalent mirror reflectivity R_M; the real part η_a corresponds to a pure metallic mirror, while the imaginary part η_b corresponds to a pure dielectric mirror. Mirror 1 is assumed to be metallic with $\eta_{sa1} = 12$ and corresponds to a 75% reflectivity, while mirrors 2 and 3 are assumed to be identical pair of pure dielectrics with $\eta_{sb2} = 25$ and correspond to 94% reflectivity.

where the third-order nonlinear dielectric susceptibility $\chi^{(3)}$ may be estimated from the classical anharmonic oscillator equation [28]

$$\chi_{iiii}^{(3)} = \frac{Nbe^4}{\varepsilon_0 m^3 \left(\omega_0^2 - \omega^2 - i\omega\Gamma \right)^4}. \tag{35}$$

In (35), N is the number density of bounded electrons, b is the nonlinear coefficient that characterizes the strength of nonlinearity, and e and m are, respectively, the charge and mass of electron. To estimate the value of $\chi_{iiii}^{(3)}$ near the resonance region from (35), we have calculated N to be 5.349×10^{28} m^{-3} for MgO. The coefficient b may then be optimized in terms of lattice constant d and ω_0 such that the static value of $\chi_{iiii}^{(3)}(\omega = 0)$ becomes $\approx 10^{-22}$ m^2/V^2, which makes $b \approx \omega_0/d^{1.7}$. For $d = 4.212 \times 10^{-10}$ m for MgO, this eventually yields a resonance value of $\chi_{iiii}^{(3)}(\omega = 0.98\omega_0) \approx 3.782 \times 10^{-17}$ m^2/V^2. With these values and utilizing (30) and (34), we obtain $\beta_s = 1.0042 \times 10^{-5}$.

Before proceeding further, it is to be noted that the numerical results presented in the following parts represent dimensionless variables (as explained in Appendix), which can easily be converted to the corresponding-dimensional ones. For example, a scaled operating frequency $f = 0.98$ corresponds to a-dimensional frequency $\omega = 0.98\omega_0 = 11.836 \times 10^{12}$ Hz where $\omega_0 = 12.18 \times 10^{12}$ Hz. Similarly, a scaled value of thickness or deflection $u = l_1$ corresponds to a dimensional value $L_1 = [c/\omega_0]l_1 = 6 \times 10^{-5}l_1$m $= 60$ μm. The dimensional value of incident electric field amplitude E_0 in V/m is obtained by multiplying the scaled value E_s by $E_0 = 10^7$ V/m, and so on.

3.3. Sensor Performance

The mathematical formulation explained in the previous section indicates that bistability in both reflectance and transmittance is basically a manifestation of bistability in polarization itself. Following the numerical procedure explained in Appendix, Fig. 3(a) presents the plot of polarization P_b at the output boundary against the absolute value of the incident electric field amplitude $|E_s|$ corresponding to different values of deflection, i.e., l_1. We observe that the system imposes a typical bistable behavior on the output light. The unique feature of these plots is that, for each value of deflection, there exists a unique threshold value of optical bistability. For example, at zero deflection [black curve in Fig. 3(a)], we notice the threshold value to occur at $|E_s| = 177$ ($|E_0| = 177 \times 10^7$ V/m). With an increase of deflection to $l_1 = 0.2$ ($L_1 = 4.926$ μm), the red curve in Fig. 3(a)
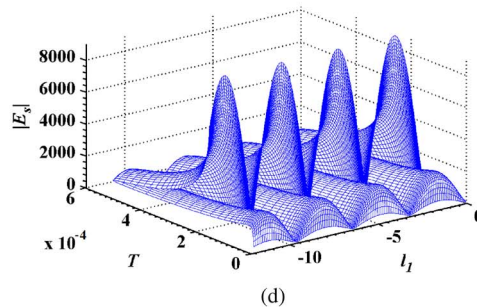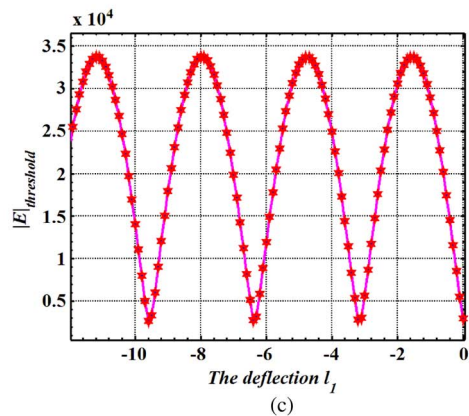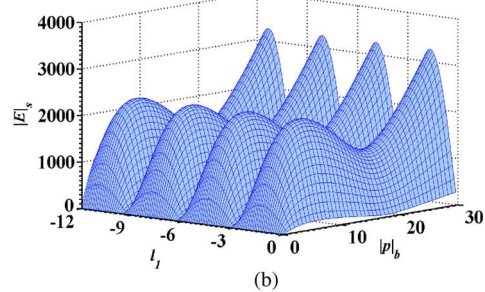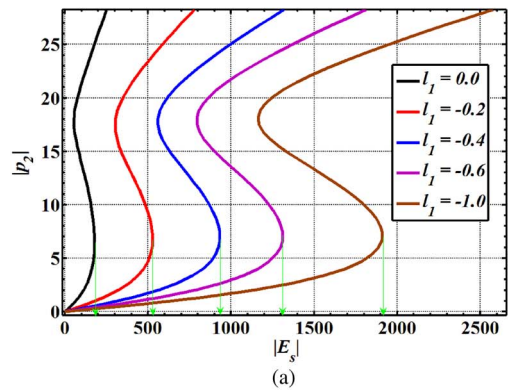
(a)

(b)

(c)

(d)

Fig. 3. (a) Plot of polarization at the output boundary against the scaled incident electric field amplitude $|E_s|$ for different values of deflection l_1. Fabry-Perot thickness l_2 is fixed at 1.6. Other parameters used are as per Sections 3.1 and 3.2. (b) Plot of polarization $|p_b|$ at the output boundary as a function of scaled incident electric field amplitude $|E_s|$ and deflection l_1. Plots show periodic patterns of optical bistability as a function of deflection l_1. Fabry-Perot thickness is fixed at $l_2 = 1.6$ as in (a). (c) Plot of threshold values of the incident electric field amplitude $|E_s|$ as a function of deflection l_1. All the used parameters remain the same as those in (a). (d) Plot of transmittance T as a function of both the incident electric field amplitude $|E_s|$ and deflection l_1. All the used parameters remain the same as those in (a).

appears with the threshold value of $|E_s| = 527$ ($|E_0| = 527 \times 10^7$ V/m). Corresponding to a further increase of deflection to $l_1 = 0.4$ ($L_1 = 9.852 \mu$ m), the blue curve in Fig. 3(a) determines a threshold value of $|E_s| = 931.5$ ($|E_0| = 931.5 \times 10^7$ V/m), and so on. Thus, it is evident that the system offers a unique threshold value for each value of applied deflection, as predicted in Refs. [5], [6]. Another feature of these curves is that the range of nonlinearity also changes in response to the change in applied deflection. For example, at a deflection of $l_1 = 0.6$ ($L_1 = 14.778 \mu$m) [purple curve in Fig. 3(a)], the nonlinear range extends from $|E_s| = 793.7$ to $|E_s| = 1310$ ($|E_0| = 7.937 \times 10^9$ to 13.10×10^9 V/m); if the deflection increases to $l_1 = 1$ ($L_1 = 24.6 \mu$m) [brown curve in Fig. 3(a)], the nonlinearity goes from $|E_s| = 1163$ to $|E_s| = 1910$ ($|E_0| = 11.63 \times 10^9$ to 19.1×10^9 V/m).

The system is then simulated over a long range of deflection. In principle, we observe that the bistability assumes some periodic pattern as a function of the applied deflection, as shown in Fig. 3(b), and (c) depicts periodic behavior of the threshold value $|E_{th}|$ of optical bistability. The periodicity in Fig. 3(c) shows that, for a specific range of deflection, say from $l_1 = 0$ to $l_1 \cong 1.5$ ($L_1 = 0$ to $L_1 \cong 36.95 \mu$m), the threshold value of optical bistability increases with the increase in applied deflection. In this range, the system exhibits a unique threshold value for each value of deflection, as explained above. If the deflection increases further, i.e., in the range from $l_1 \cong 1.5$ to $l_1 \cong 3.0$ (corresponding to $L_1 = 36.95 \mu$m to 73.89μm), we observe that the threshold values of system decreases (upon increasing the deflection). In the range from $l_1 \cong 3.0$ to $l_1 \cong 4.7$ (corresponding to $L_1 \cong 73.89 \mu$m to 115.76μm), threshold values increase again upon increasing the applied deflection, and so on. The above analysis indicates that the system works well within a specific range of deflection. For system design chosen in our simulation, the optimum range lies around $L_1 \approx 100 \mu$m. In considerably higher ranges than this, the possibility increases of having a similar bistable response and threshold values, affecting thereby the sensitivity of sensor. The periodicity in bistable behavior appears in the transmittance T as well as when observed as a function of applied deflection [see Fig. 3(d)]. This is very much expected as the bistability in both reflectance R and transmittance T is just a manifestations of bistability in polarization itself, as indicated in (A.4) and (A.5) in the Appendix.

In the case of relatively large thickness values of nonlinear medium, the system exhibits multistable behavior [see Fig. 4(a)]. For example, in the case when there is no deflection ($l_1 = 0$), only one line curve (black curve) exists with three different threshold points. The first threshold value (point a) occurs at $|E_s| = 382$ ($|E_0| = 382 \times 10^7$ V/m) while the second (point b) and the third (point c) threshold values occur at $|E_s| = 690$ ($|E_0| = 690 \times 10^7$ V/m) and $|E_s| = 1508$ ($|E_0| = 1508 \times 10^7$ V/m), respectively. When the deflection is induced to $l_1 = -0.2$, the red curve appears with a new set of threshold values (points d, e and f). In this case, both the black and the red curves present illustrative threshold points a, b, c, d, e, and f. Alternatively, if further deflection is induced up to $l_1 = -0.4$, the system threshold jumps to points g, h and i on the blue curve. If the deflection vanishes, the output remains at the last three points; the patterns of curves can be well understood—the kind that will continue if further deflection is induced into the system.

In addition to the idea of memorizing a previous deflection, threshold values do not always increase as a function of deflection, but rather moves back and forth. In general, we have simulated the system from zero deflection up to a value of $l_1 = 12$ [see Fig. 4(b)], and found that the system still depicts the same periodic pattern as a function of deflection even in the case of multistability. This is attributed to the constructive and destructive interference occurring in the first resonator. That is, when the deflection occurs, the thickness of the first resonator changes, which may lead to either a constructive or destructive interference. In the case of constructive interference, the input signal from the first resonator increases. On the other hand, in the case of destructive interference, the output intensity from the first resonator remains the minimum. If the difference between the phases remains intermediate between these two extremes, the magnitude of input signal lies between the minimum and the maximum values.
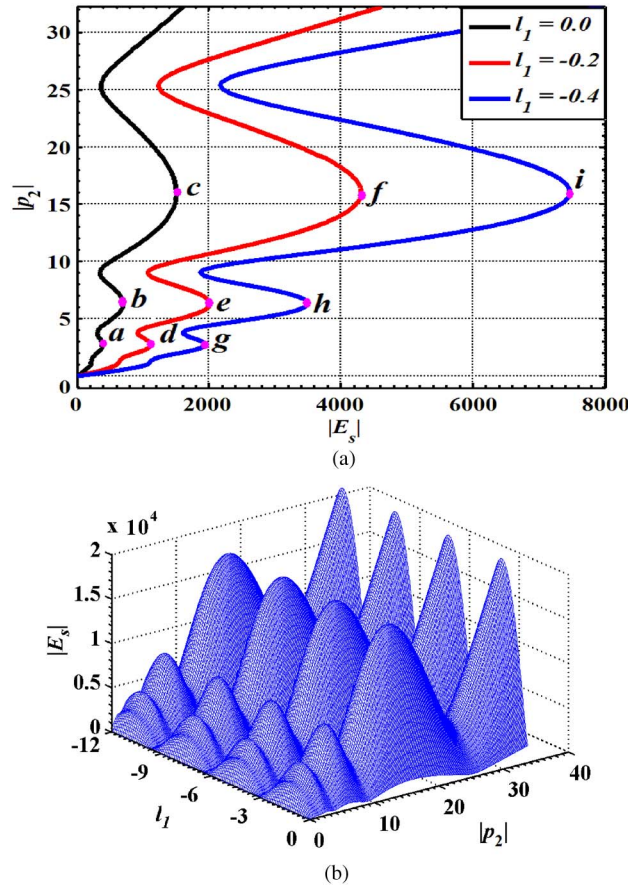
Fig. 4. (a) Optical multistability of polarization $|p_b|$ as a function of incident electric field $|E_s|$ at three different values of deflection l_1. Fabry-Perot thickness is fixed at $l_2 = 20$. Other parameters are as per Sections 3.1 and 3.2. (b) Optical multistability of polarization $|p_b|$ as a function of incident electric field $|E_s|$. Multistability shows a periodic pattern as a result of gradual increase of deflection l_1. Fabry-Perot thickness is fixed at $l_2 = 20$ as in (a).

4. Conclusion

The functionality and performance of a photonic deflection sensor is investigated using Maxwell-Duffing approach that implements the electric field of wave equation to be expressed as a nonlinear function of polarization using the Duffing anharmonic equation, and the resulting nonlinear polarization equation is solved across the nonlinear medium. Expressions for both reflectance and transmittance are obtained as functions of the nonlinear polarization and other material parameters. Results reveal that the system assumes a new threshold value in response to each applied deflection. Also, the system offers a memory effect through remembering the previous applied deflection. In addition, the threshold value of optical bistability depicts a periodic pattern as a function of applied deflection. Such a periodicity can be understood in the view of constructive and destructive interference in the first resonator due to the varying resonator thickness. This, in turn, changes the input intensity of the second resonator as a result of the applied deflection, and eventually changes the output optical bistability. The periodicity in bistability threshold suggests the efficacy of the system to lie within a range of deflection from zero to 1.5 times of the operating wavelength. If the deflection increases to multiple values of operating wavelength, the possibility of the system to repeat the same threshold values increases.

Appendix
Scaling and Numerical Procedure

To numerically simulate the system, it is more convenient to scale the relevant equations and deal numerically with the scaled variables rather than the dimensional ones. Therefore, (7) can be scaled using the variables in (30) to the following dimensionless equation:

$$\left[|\rho_s|^2 + 2\beta_s(\rho_s + \rho_s^*)|p|^2 + 3\beta_s^2|p|^4\right]\frac{d^2p}{du^2} = -2\beta_s\left[\rho_s^* + 2\beta_s|p|^2\right]p^*\left(\frac{dp}{du}\right)^2 + 2\beta_s^2 p^3\left(\frac{dp^*}{du}\right)^2$$

$$-4\beta_s\left[\rho_s^* + \beta_s|p|^2\right]p\frac{dp}{du}\frac{dp^*}{du} - \varepsilon_\infty f^2\left\{\rho_s^*(\rho_s + w^2) + \beta_s(2\rho_s + w^2)|p|^2 + \beta_s^2|p|^4\right\}p. \quad \text{(A.1)}$$

In (A.1), the other scaled parameters are $w^2 = \gamma/\varepsilon_0\varepsilon_\infty\omega_0^2 = \omega_p^2/\varepsilon_\infty\omega_0^2$ and $\rho_s = 1 - f^2 - ifg$. Since there is no incoming wave in the transmission medium 4, it is convenient to integrate (A.1) from $u = l_2$ to $u = 0$. Thus, the numerical calculation begins by giving an arbitrary initial value of polarization $p_2 = p_2^*$ at the boundary $u = l_2$. Next, the derivative dp_2/du and its complex conjugates dp_2^*/du are calculated using the following scaled equation:

$$\frac{dP_2}{dz} = -ifp_2\left\{\frac{3}{4}\beta_s(n_4 + \eta_{3s}^*)|p_2|^2\left[\rho_s^* + \frac{3}{4}\beta_s|p_2|^2\right] + (n_4 + \eta_{3s})\left[\rho_s^* + \frac{3}{2}\beta_s|p_2|^2\right]\left[\rho_s + \frac{3}{4}\beta_s|p_2|^2\right]\right\}$$

$$\left/\left\{\left[\rho_s + \frac{3}{2}\beta_s|p_2|^2\right]\left[\rho_s^* + \frac{3}{2}\beta_s|P_2|^2\right] - \frac{9}{16}\beta_s^2|p_2|^4\right\}\right. . \quad \text{(A.2)}$$

Equation (A.2) is the scaled version of (28). Subsequently, (A.1) is integrated from the interface $u = l_2$ to $u = 0$ to obtain p_1. The integration process keeps tracks of polarization across the nonlinear medium. The procedure is repeated for a large number of arbitrary p_2 values. The resulting polarization p_1 is then used to evaluate the scaled incident electric field amplitude E_s and the reflectance $R = |r|^2$ using the following scaled equations:

$$E_s = \frac{-1}{4f^2\gamma_s n_1 n_2 \delta_1^-}\left\{if\left(\hbar_{1s}^-\delta_2^+ - \hbar_{1s}^+\delta_2^-\right)\left[\frac{3}{4}\beta_s p^2\frac{dp_1^*}{du} + \rho_s\frac{dp_1}{du} + \frac{3}{2}\beta_s|p_1|^2\frac{dp_1}{du}\right]\right.$$

$$\left. + f^2\left[\eta_{2s}\left(\hbar_{1s}^-\delta_2^+ - \hbar_{1s}^+\delta_2^-\right) - n_2\left(\hbar_{1s}^-\delta_2^+ + \hbar_{1s}^+\delta_2^-\right)\right]\left[\rho_s + \frac{3}{4}\beta_s|p_1|^2\right]p_1\right\} \quad \text{(A.3)}$$

$$r = \left[\frac{2n_1 - \hbar_{1s}^-}{\hbar_{1s}^-}\right]\frac{\delta_1^-}{\delta_1^+} - \frac{1}{\delta_1^+}\left[\frac{2n_2}{\hbar_{1s}^-\delta_2^+ - \hbar_{1s}^+\delta_2^-}\right]\left[\frac{1}{\gamma_s E_s}\left(\rho_s + \frac{3}{4}\beta_s|p_1|^2\right)p_1 - \frac{2n_1}{\hbar_{1s}^+}\frac{\delta_1^-}{\delta_2^+}\right]. \quad \text{(A.4)}$$

Equations (A.3) and (A.4) are the scaled versions of (27) and (29), respectively, and the newly introduced scaled variables are

$$\gamma_s = \gamma E_0/\omega_0^2 P_0, \qquad \eta_s = c\mu_0\eta, \qquad \hbar_{1s}^- = (n_1 - n_2 + \eta_{1s}), \qquad \hbar_{1s}^+ = (n_1 + n_2 + \eta_{1s})$$
$$\delta_1^+ = \exp(ifn_1 l_1), \quad \delta_1^- = \exp(-ifn_1 l_1), \quad \delta_2^+ = \exp(ifn_2 l_1), \quad \text{and} \quad \delta_2^- = \exp(-ifn_2 l_1)$$

where n_1 and n_2 are the RIs of the mediums 1 and 2, respectively. Finally, the transmission coefficient t may be evaluated using the equation

$$t = \frac{1}{E_s\gamma_s\delta_4^+}\left[\rho_s + \frac{3}{4}\beta_s|p_2|^2\right]p_2 \quad \text{(A.5)}$$

where $\delta_4^+ = \exp(ifn_4 l_2)$ with n_4 being the RI of the medium 4. We found that the use of variable-step solver of an explicit Runge-Kutta method produces more accurate results, and the input/output curves are generated naturally without fitting or interpolation to the data.

Acknowledgment

The authors are indebted to the two anonymous reviewers for constructive criticisms on the manuscript, which greatly helped to improve the status of it.

References

[1] J. Haus, *Optical Sensors: Basics and Applications*.   Weinheim, Germany: Wiley-VCH Verlag Gmbh & Co. KgaA, 2010.
[2] Optical Sensors, E. Wagner, R. Dändliker, and K. Spenner, Eds.   Weinheim, Germany: Wiley-VCH, 2008.
[3] R. Narayanaswamy and O. S. Wolfbeis, *Optical Sensors: Industrial, Environmental and Diagnostic Applications*.   New York, NY, USA: Springer-Verlag, 2004.
[4] J. Fraden, *Handbook of Modern Sensors: Physics, Design and Applications*.   Berlin, Germany: Springer-Verlag, 1996.
[5] S. H. Shehadeh, M. Cada, M. Qasymeh, and Y. Ma, "Multistable cascaded optical resonators for deflection sensors," *IEEE Sensors J.*, vol. 11, no. 9, pp. 1899–1904, Sep. 2011.
[6] S. H. Shehadeh, M. Cada, Y. Ma, and M. Qasymeh, "Application of optical multi-stability to deflection sensors," in *Proc. WCECS*, 2009, vol. I, pp. 531–534.
[7] J. H. Marburger and F. S. Felber, "Theory of a lossless nonlinear Fabry-Perot interferometer," *Phys. Rev. A*, vol. 17, no. 1, pp. 335–342, Jan. 1978.
[8] Y. R. Shen, *The Principles of Nonlinear Optics*.   New York, NY, USA: Wiley, 1984.
[9] W. Chen and D. Mills, "Optical response of a nonlinear dielectric film," *Phys. Rev. B*, vol. 35, no. 2, pp. 524–532, Jan. 1987.
[10] J. Goldstone and E. Garmire, "Intrinsic optical bistability in nonlinear media," *Phys. Rev. Lett.*, vol. 53, no. 9, pp. 910–913, Aug. 1984.
[11] K. H. Chew, J. Osman, and D. R. Tilley, "The nonlinear Fabry-Perot resonator: Direct numerical integration," *Opt. Commun.*, vol. 191, no. 3–6, pp. 393–404, May 2001.
[12] R. E. Mickens, "Mathematical and numerical study of the Duffing-harmonic oscillator," *J. Sound Vibration*, vol. 244, pp. 563–567, Jul. 2001.
[13] H. M. Gibbs, S. L. McCall, and T. N. C. Venkatesan, "Differential gain and bistability using a sodium-filled Fabry-Perot interferometer," *Phys. Rev. Lett.*, vol. 36, no. 19, pp. 1135–1138, May 1976.
[14] H. M. Gibbs, S. L. McCall, T. N. C. Venkatesan, A. C. Gossard, A. Passner, and W. Wiegmann, "Optical bistability in semiconductors," *Appl. Phys. Lett.*, vol. 35, no. 6, pp. 451–453, Sep. 1979.
[15] H. M. Gibbs, *Optical Bistability: Controlling Light With Light*.   Orlando, FL, USA: Academic, 1985.
[16] G. Vitrant, M. Haelterman, and R. Reinisch, "Transverse effects in nonlinear planar resonators II. Modal analysis for normal and oblique incidence," *J. Opt. Soc. Amer. B*, vol. 7, no. 7, pp. 1319–1327, Jul. 1990.
[17] C. M. Bowden and C. C. Sung, "First- and second-order phase transitions in the Dicke model: Relation to optical bistability," *Phys. Rev. A*, vol. 19, no. 6, pp. 2392–2401, Jun. 1979.
[18] M. Hehlen, H. U. Güdel, Q. Shu, J. Rai, S. Rai, and S. C. Rand, "Cooperative bistability in dense, excited atomic systems," *Phys. Rev. Lett.*, vol. 73, no. 8, pp. 1103–1106, Aug. 1994.
[19] R. Murgan, D. R. Tilley, Y. Ishibashi, J. F. Webb, and J. Osman, "Calculation of nonlinear-susceptibility tensor components in ferroelectrics: Cubic, tetragonal, and rhombohedral symmetries," *J. Opt. Soc. Amer. B*, vol. 19, no. 9, pp. 2007–2021, Sep. 2002.
[20] A.-B. M. Ibrahim, D. R. Tilleya, and J. Osmana, "Optical bistability from ferroelectric Fabry-Perot interferometer," *Ferroelectrics*, vol. 355, no. 1, pp. 140–144, 2007.
[21] A. -B. M. A. Ibrahim and J. Osman, "Intrinsic optical bistability in Kerr ferroelectric materials," *Eur. Phys. J. B*, vol. 63, no. 2, pp. 193–198, May 2008.
[22] M. Born and E. Wolf, *Principles of Optics: Electromagnetic Theory of Propagation, Interference and Diffraction of Light*.   Oxford, U.K.: Pergamon, 1980.
[23] S.-C. Lim, J. Osman, and D. R. Tilley, "Theory of a gyromagnetic Fabry-Pérot resonator," *J. Phys., Cond. Matt.*, vol. 9, no. 39, pp. 8297–8306, Sep. 1997.
[24] A. -B. M. A. Ibrahim, "Optical bistability in nonlinear Kerr dielectric and ferroelectric materials," Ph.D. dissertation, Univ. Sains Malaysia, Pulau Penang, Malaysia, 2009.
[25] C. F. Bohren and D. R. Huffman, *Absorption and Scattering of Light by Small Particles*.   Hoboken, NJ, U: Wiley-VCH, 2008.
[26] J. Han, B. K. Woo, W. Chen, M. Sang, X. Lu, and W. Zhang, "Terahertz dielectric properties of MgO nanocrystals," *J. Phys. Chem. C*, vol. 112, no. 45, pp. 17 512–17 516, 2008.
[27] J. Osman, Y. Ishibashi, and D. R. Tilley, "Calculation of nonlinear susceptibility tensor components in ferroelectrics," *Jpn. J. Appl. Phys.*, vol. 37, no. 9A, pp. 4887–4893, Sep. 1998.
[28] R. W. Boyd, *Nonlinear Optics,* 3rd ed.   Orlando, FL, USA: Academic, 2008.